Biodegradation of Iron Oxide Nanocubes: High-Resolution *In Situ* Monitoring

Lénaic Lartigue,[†,‡] Damien Alloyeau,[‡,*] Jelena Kolosnjaj-Tabi,[†,§] Yasir Javed,[‡] Pablo Guardia,[⊥] Andreas Riedinger,[⊥] Christine Péchoux,[∥] Teresa Pellegrino,[⊥] Claire Wilhelm,[†] and Florence Gazeau[†,*]

[†]Laboratoire Matières et Systèmes Complexes, UMR 7057, and [‡]Laboratoire Matériaux et Phénomènes Quantiques, UMR 7162, CNRS/Université Paris Diderot, 10 rue Alice Domon et Léonie Duquet, F-75205 Paris Cedex 13, France, [§]Inserm U970, Paris Cardiovascular Research Center-PARCC/Université Paris-Descartes, 56 rue Leblanc, 75015 France, [⊥]Istituto Italiano di Tecnologia, via Morego 30, 16163 Genova, Italy, and [∥]UR1196 Génomique et Physiologie de la Lactation, INRA, Plateau de Microscopie Electronique 78352 Jouy-en-Josas, France

ABSTRACT The long-term fate of nanomaterials in biological environment represents a critical matter, which determines environmental effects and potential risks for human health. Predicting these risks requires understanding of nanoparticle transformations, persistence, and degradation, some issues somehow ignored so far. Safe by design, inorganic nanostructures are being envisioned for therapy, yet fundamental principles of their processing in biological systems, change in physical properties, and *in situ* degradability have not been thoroughly assessed. Here we report the longitudinal visualization of iron oxide nanocube transformations inflicted by the intracellular-like environment. Structural degradation of individual nanocubes with two different surface coatings (amphiphilic polymer shell and polyethylene glycol ligand molecules) was monitored at the atomic scale with aberration-corrected high-resolution transmission electron microscopy. Our results suggest that the polymer coating controls surface reactivity and that availability and access of chelating agents to the crystal surface govern the degradation rate. This *in situ* study of single nanocube degradation was compared to intracellular transformations observed in mice over 14 days after intravenous injection, revealing the role of nanoparticle clustering, intracellular sorting within degradation compartments, and iron transfer and recycling into ferritin storage proteins. Our approach reduces the gap between *in situ* nanoscale observations in mimicking biological environments and *in vivo* real tracking of nanoparticle fate.

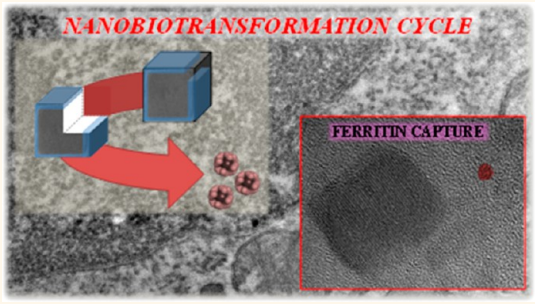

KEYWORDS: bio-nano interactions · nanomedicine · environmental · health and safety issue · degradation · nanomagnetism

The increasing development of nanomaterials with physical properties that are specific to their nanometer scale has generated important concerns about their fate and impacts to the environment. Safe implementation of engineered nanoparticles for industrial purposes as well as nanomedicine requires a comprehensive understanding of their behavior in living organisms and particularly in humans. A consequence of nanoparticle's high surface-to-volume ratio is their propensity to suffer chemical and physical transformation, degradation, and corrosion triggered by interactions with the surrounding medium.[1,2] Biologically mediated transformations are even more complex, as they involve interactions with a variety of biomolecules and, in turn, also affect the physical state (aggregation and physical properties) and chemical evolution of nanomaterials.[3] Therefore, providing an in-depth insight into the reactivity nanoparticles within biological media they will encounter is a prerequisite for designing safe nanomedical products. Just as surface reactivity is essential to catalysis applications,[4] it is also a crucial underestimated determinant of nanoparticle outcome in the organism and potential hazard for human health. Some transformations of inorganic nanomaterials have been identified as critical factors determining their transport, persistence, and toxicity in biological media. Reduction or oxidation of elemental metal and metal oxide nanoparticles occurs in natural systems through interactions with various ligands and may lead to the crystal dissolution and release of toxic

* Address correspondence to florence.gazeau@univ-paris-diderot.fr, damien.alloyeau@univ-paris-diderot.fr.

Received for review December 11, 2012 and accepted May 1, 2013.

Published online May 01, 2013
10.1021/nn305719y

soluble ions, such as Ag^+, Fe^{2+}, or Zn^{2+}.[5,6] Nanoparticle shape and surface reactivity have been shown recently to influence cytotoxicity through the role of crystal defects which catalyze biological injury.[7] Conversely, other mechanisms may limit crystal core dissolution and increase bioaccumulation and persistence of nanoparticles. Commonly used capping agents (*i.e.*, inorganic coating) as well as small and large organic molecules raise a first barrier against environmental reagents, which may affect and delay the crystal reactivity. Adsorption of biomacromolecules on nanoparticles—the so-called protein corona—also plays a critical role as it changes the biological identity of nanomaterials which are seen by cells and dynamically modifies the interface with the environment.[8,9] Pharmacokinetic, macrophage uptake, and biodistribution of parenterally administrated nanoparticles are profoundly affected by protein adsorption which also may vary over the journey of nanoparticles in the organism.[10,11] Another important element for nanoparticle fate is their tendency to agglomerate in the biological environment, which may be due to chemical destabilization, release of capping agent, and adsorption of host macromolecules.[12,13] Moreover, most inorganic nanomaterials interacting with cells end up confined in intracellular compartments—the lysosomes, where they are exposed to the combined effect of acidic pH (around 4.7), lysosomal digestive enzymes, and iron chelators involved in iron regulation.[14] It is generally assumed that the biotransformation of nanoparticles could take place in such an environment.[15−17] Recently, by monitoring the magnetic signature of iron oxide spherical nanoparticles proposed as MRI contrast agent, we evidenced the crucial role of capping agent in the kinetics of their degradation.[18] Moreover, after injection to the animal, we demonstrated their intracellular clustering[19] and degradation over months, which resulted in iron recycling into ferritin storage protein.[20] However, the intimate mechanisms of single-particle degradation remain unknown, mainly because of the difficulty to visualize a single particle over time along with its bioenvironment. Considering the multiple factors which influence nanoparticle biodegradation and biopersistence, there is a need for methods to investigate these processes at the relevant scales—especially the nanometer scale—and in biologically relevant environments. Here we propose an approach to reduce the gap between *in situ*, *in vitro*, and *in vivo* observations of nanoparticle fate. The rate and extent of nanoparticle transformations was monitored over time and at the atomic scale, under conditions of increasing complexity: in a minimal biomimetic degradation medium, within *in vitro* cells, and directly *in vivo* on specific organs (liver and spleen) where nanoparticles accumulate after intravenous injection. In this study, we investigated for the first time the *in situ* morphological transformation of single iron oxide nanocubes having different surface coatings in a medium mimicking intracellular lysosomal environment. The kinetics of structural degradation was monitored with aberration-corrected high-resolution transmission electron microscopy (HRTEM). With the same atomic precision, we then confronted *in situ* findings to the *in vivo* biotransformation of nanocubes after intravenous injection in mice.

RESULTS AND DISCUSSION

In order to visualize conspicuous change in the nanoparticle's morphology, we chose superparamagnetic iron oxide (maghemite or magnetite) nanocrystals with a characteristic cubic shape. Iron oxide nanocubes have been highlighted recently as outstanding mediators for magnetically induced cancer hyperthermia[21−23] and magnetic resonance imaging.[24,25] Apart from their unique theranostic efficiency, the bioprocessing of magnetic nanocubes and the persistence of their physical properties in the organism remain unexplored. Nanocubes of 21 nm edge length (Figure 1A) were synthesized by a thermal decomposition method.[21] Shape control was achieved by the selective interactions of surfactant molecules (decanoic acid) with preferential growth facet (Figure 1B).[26] Initial HRTEM observations of nanocubes (Figure 1B) show monocrystals bound by {400} facets and small {220} facets at the edges with the inverse spinel structure (face-centered cubic unit cell with the *Fd*3*m* space group).[26,27] We note that nanocubes with the vacancy-ordered γ-Fe_2O_3 structure (tetragonal unit cell with the $P4_12_12$ space group) were also observed.[27−29] The hydrophobic nanocrystals were then transferred to water by intercalation of an amphiphilic polymer (poly(maleic anhydride-*alt*-1-octadecene, 30−50 kDa) resulting in a micelle-like coating, which also ensured colloidal stability (Figure 1C and Supporting Information Figure S1).[30,31] Alternatively, through the ligand exchange procedure, the same nanocube precursor could be coated with poly(ethylene glycol)-gallol (PEG-gallol, 3 kDa),[32] using the high binding affinity of gallic acid (a catechol-derived anchor) for the iron oxide (Figure 1C). These PEG-coated nanocubes with high stability in physiological medium were specially designed for *in vivo* injection in order to limit protein adsorption and prolong circulation time.[33] In order to induce degradation, nanoparticles were exposed to an aqueous buffer medium at pH 4.7 containing citrate ions (20 mM) as iron chelator.[18] This medium was first proposed by Arbab *et al.*[16] to mimic lysosomal environment.

Follow-up of Nanocube Monolayers on Lacey Carbon Film in the Presence of the Lysosome-like Medium. The kinetic of nanoparticle transformation was investigated at atomic level using aberration-corrected HRTEM on nanoparticles flatly deposited on a lacey carbon-coated TEM grid. The grid was immersed into the buffer medium for

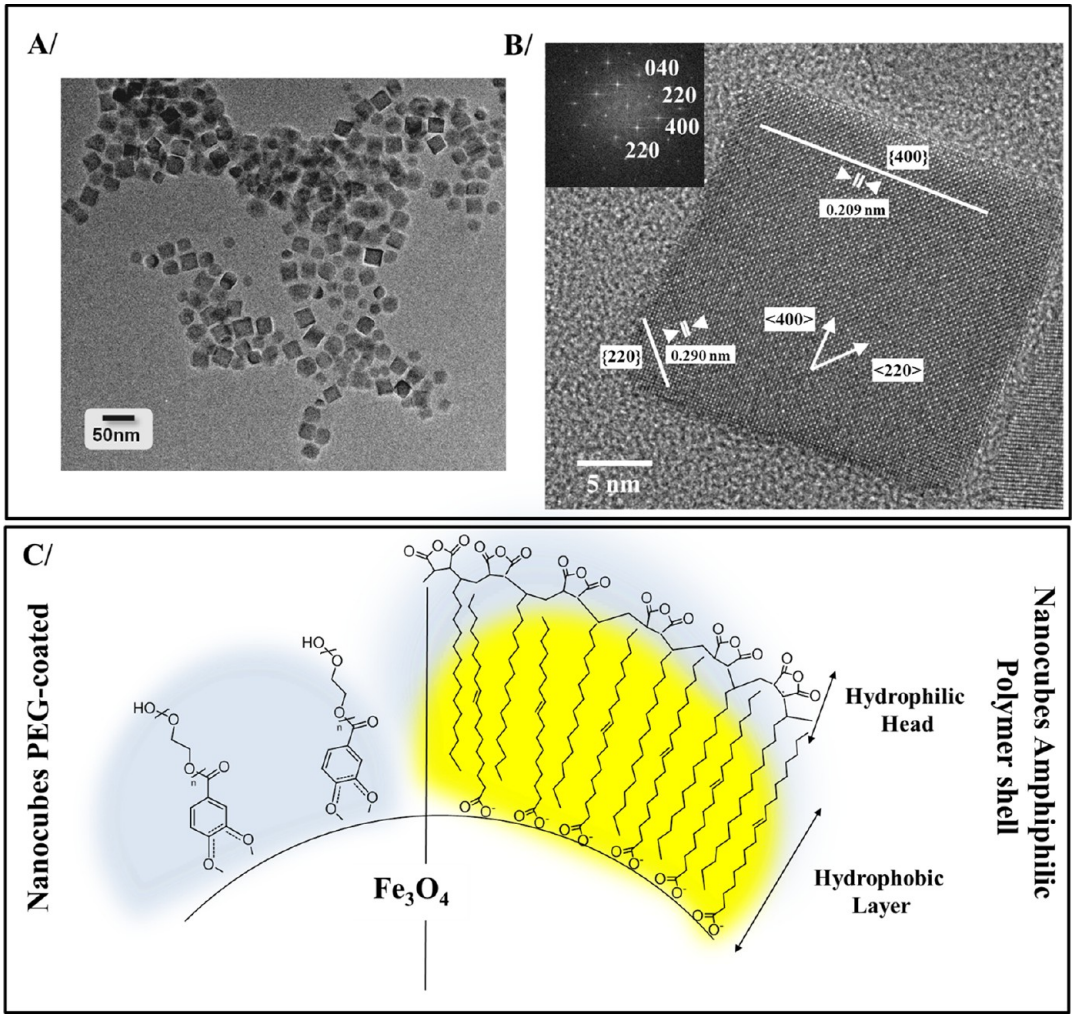

Figure 1. Description of iron oxide nanocubes used in the study. (A) Micrograph of initial nanoparticles in water suspension. (B) Atomic-resolution images (with the corresponding fast Fourier transform (FFT) in the inset) of an amphiphilic polymer-coated nanocube in its initial state. From the FFT, the inverse spinel structures with an interplanar distance of 2.90 and 2.09 Å for the {220} and {400} planes, respectively, were found. (C) Sketch of the different surface coatings. On the right, the as-synthesized hydrophobic nanoparticles with decanoic acid at their surface could be transferred in water by intercalation of an amphiphilic polymer (poly(maleic anhydride-*alt*-1-octadecene) resulting in a micelle-like coating. On the left, the surfactant molecules at the nanoparticle surface were displaced by poly(ethylene glycol)-gallol molecules through a ligand exchange procedure. Gallol, a derivative of catechol, serves as a strong anchor for the iron oxide surface.

different time periods, and the nanoparticle evolution was probed after each immersion step. First, about 300 isolated nanocubes were localized on the grid and identified to monitor their degradation (Supporting Information Figure S2 gives example of the localization procedure). In the lysosome-like medium, morphological transformations occurred within the first 30 min of immersion (Figure 2). Ninety-nine percent of isolated nanocubes were damaged in comparison to their initial state after 90 min for nanocubes with an amphiphilic polymeric shell and after only 40 min for the PEG-coated nanocubes (Figure 2A–D). Initial attack of nanoparticles induced in most cases complete dissolution. The proportion of totally dissolved nanoparticles increased from 3% after 30 min to 23% after 60 min for the amphiphilic shell nanocubes. In the case of PEG-coated particles, during the same time, this proportion rises from 3 to 70%. Morphology of the particles with an amphiphilic shell did not evolve after 300 min, which leads to the conclusion that a stable state was reached (Supporting Information Figure S3). Observations at the nanometer level also reveal the importance of the particle aggregation on the degradation mechanisms. We frequently observed aggregates of nanocubes on the lacey film. As shown in Figure 2E,F, localized damage occurred within the first minutes of immersion in the acidic medium, affecting first the particles at the cluster periphery. The degradation of PEG-coated nanocubes was delayed in the center of the aggregates but still occurs within a few hours (Figure 2F). In contrast, clusters of nanocubes embedded in the amphiphilic shell tended to contract and no further degradation was observed. As observed in Figure 2E, the amphiphilic shell was somehow reshaped over the aggregate and

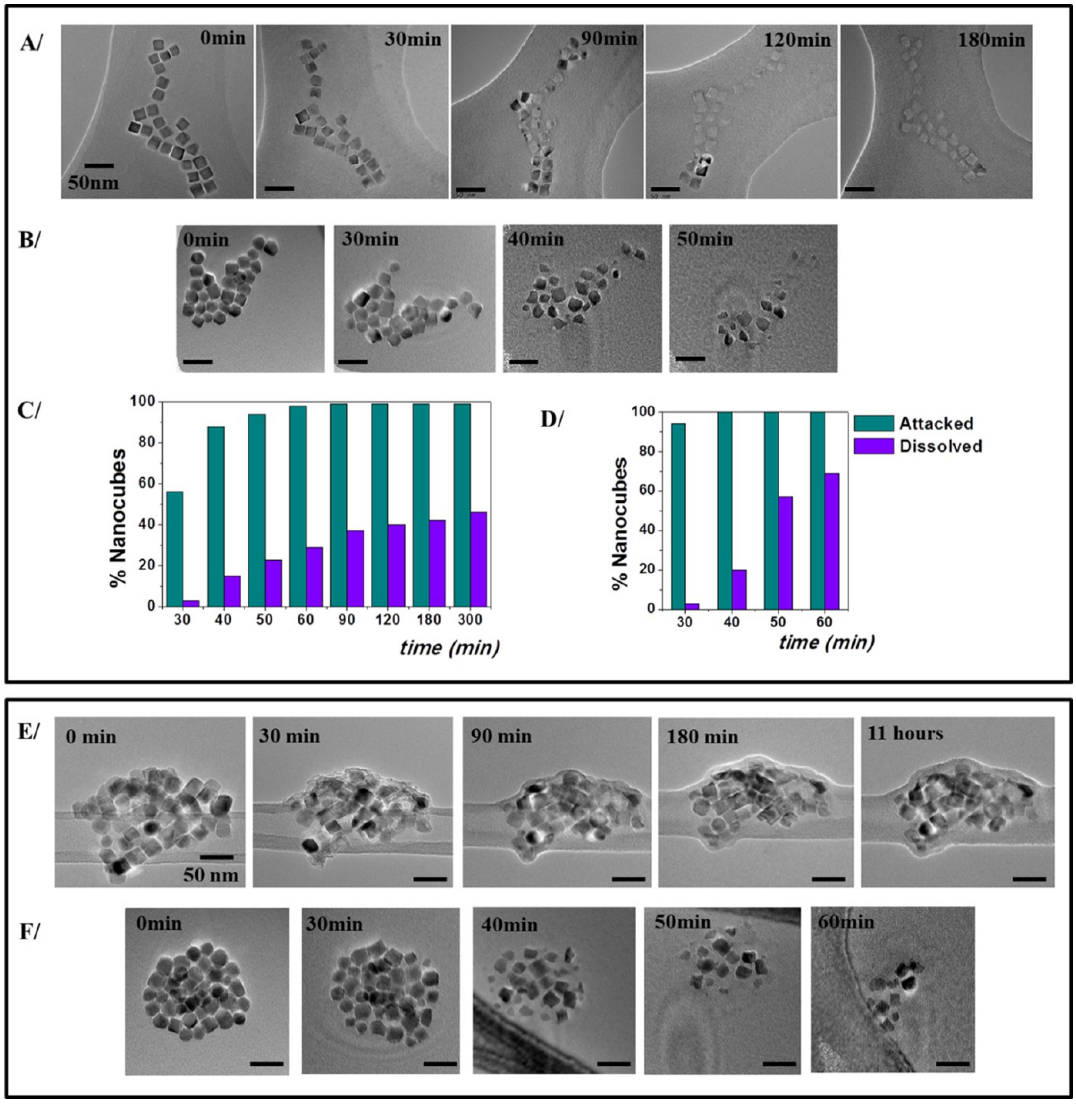

Figure 2. TEM monitoring of nanocube degradation in a lysosome-like medium. (A,B) TEM monitoring of a monolayer of nanocubes with amphiphilic polymer shell (A) or coated with PEG (B) in the lysosome-like medium. The nanoparticles which are cubic in the initial state are gradually eroded and even totally dissolved after 3 h in the lysosome-like medium. The footprints of the polymer shell which coats the particles are still observed on micrograph at 120 min, while the iron oxide crystal totally vanished. (C,D) Evolution of the percentage of attacked (green) *vs* totally dissolved nanocubes (violet) over time of incubation in the lysosome-like medium (n = 300) for nanocubes with amphiphilic shell (C) or PEG coating (D). (E,F) Follow-up of a single three-dimensional aggregate of nanocubes with amphiphilic shell (E) or PEG coating (F) over time. Note the difference in time scale. The nanocubes with the an amphiphilic shell show the onset of degradation when localized at the edge of the aggregates followed by rearrangement, likely due to polymer redistribution. The aggregate finally reaches a stable state, owing to the protective layer of the shell. In contrast, the PEG-coated nanocubes in the aggregate dissolve over the first hour. Nanocubes at the periphery of the aggregates are more rapidly degraded. Comparing panels B and F, we note that the degradation is faster in monolayers of nanocubes (B) in comparison to spherical aggregates that offer the minimum possible surface to the external environment for chemical attack.

consequently ensured an efficient protection of the assembly over time. This phenomenon highlights the dynamical redistribution of the micelle-like coating during the degradation process, which could account for the persistence of some recomposed aggregates and of polymer-stabilized anisotropic nanocube leftovers (Supporting Information Figure S3). Moreover, to verify the polymer stability in the lysosome-mimicking media, an additional control experiment on "empty" micelles of amphiphilic polymer (no iron oxide particle associated with them) was carried out. The comparison of NMR measurements on empty micelles kept in PBS buffer at pH 9 and in acidic citrate solution at pH 4.7 for 10 and 24 h showed no change in the NMR spectra, thus suggesting no trace of degradation of the polymer at different time points (see Supporting Information Figure S4). This observation also supports the retarded degradation kinetics of polymer-coated nanocubes.

To gain insight into the mechanisms ruling the degradation of nanocubes with the amphiphilic polymer, the phenomenon was followed at the single-nanoparticle scale. Aberration-corrected HRTEM allowed monitoring

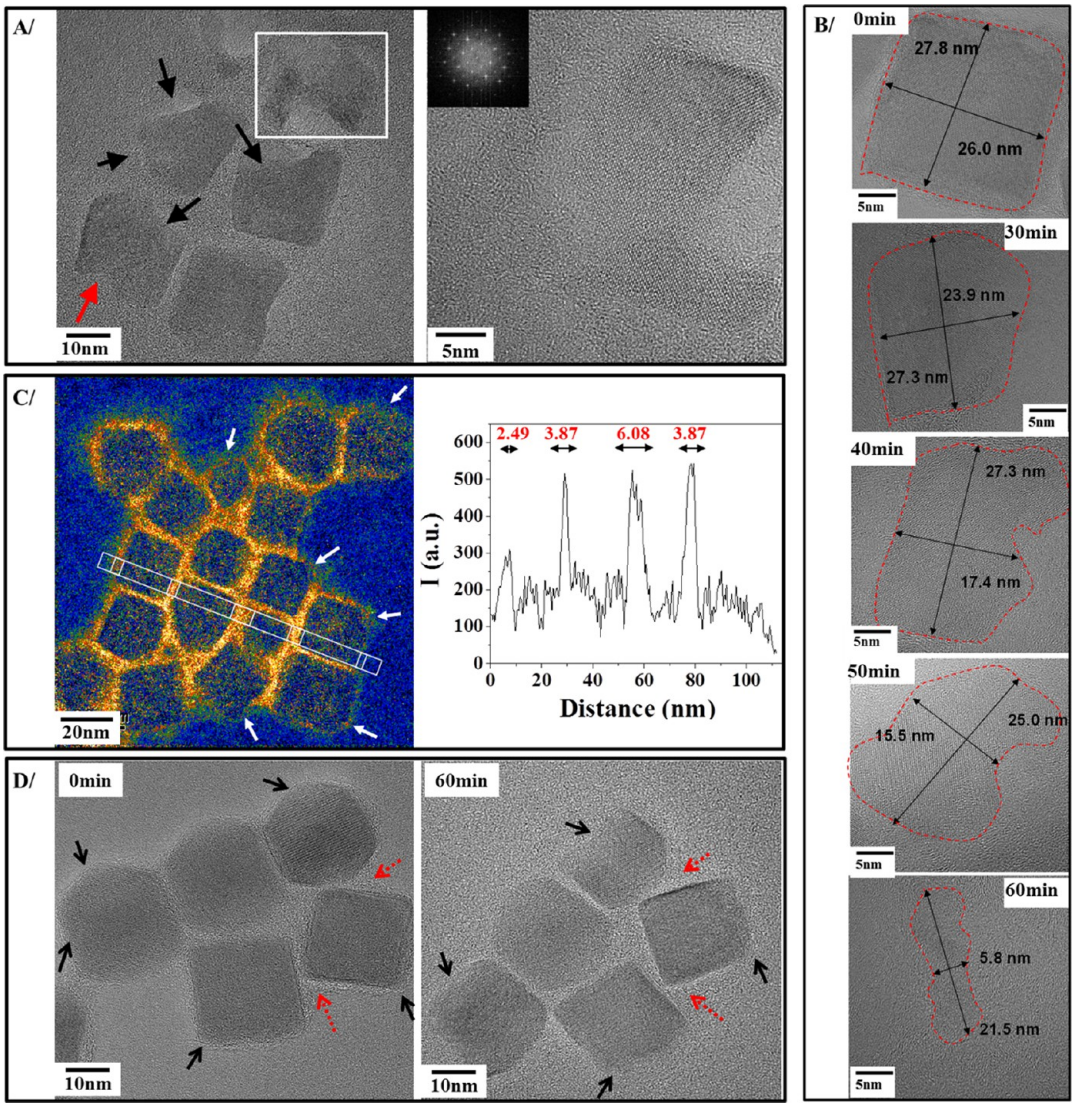

Figure 3. Role of the amphiphilic polymer coating in the degradation of nanocubes. (A) Onset of degradation localizes at different sites of the crystal. Left: nanocubes attacked on the {220} plane (black arrows) or on the {400} plane (red arrow). Right: Atomic resolution of the nanocube enclosed in the white square and FFT transform in inset, showing the persistence of the initial spinel inverse crystal structure. (B) Sixty minute follow-up of a single cube. Starting from some damaged edges, the crystal is eroded randomly, producing irregular and anisotropic contours. (C) Imaging the nanocubes/polymer interface. Left: Carbon mapping acquired by EFTEM on the carbon K-edge (284 eV) and extracted by using the three windows technique. Here, the nanocubes were not degraded and were deposited on an amorphous silicone-coated microscope grid in order to extract the carbon signal stemming only from the polymer. The arrows indicate the nanocube surfaces that are not covered by the polymer. The white rectangle represents the integrated area for plotting the intensity profile (right). The profile clearly highlights the absence of polymer on the outside right nanocube, while the others present a polymer layer between 2.5 nm on the free side and 6 nm between nanocubes. (D) Pattern of degradation onset colocalizes with faults in the polymer coating around particles. Left: Black arrows indicate the nanocube regions that were initially not covered by the polymer, and the red-dashed arrows indicate the polymer-protected surfaces. Right: Black arrows point out the nanocube surfaces that have been attacked after 60 min in the lysosome-like medium, whereas the red-dashed arrows show intact surfaces.

of the evolution of the nanoparticle's atomic structure with an unprecedented resolution and without delocalization of the atomic contrast, providing a clear visibility of the nanocrystal surfaces (Figure 3). Remarkably, the initial atomic arrangement of nanoparticles was maintained throughout the degradation process (Figure 3A,B). The morphological evolution shown in Figures 2A and 3B illustrates the continuous change of the nanoparticle's shape upon degradation. Interestingly, the dissolution did not occur layer-by-layer on a preferential atomic plane but raised into the crystal in directions which were not necessarily correlated to the crystalline axes. As a consequence, some rough uneven interfaces could be observed, without recollection of the original cube shape but still maintaining the initial crystal lattice (Figure 3A). Once an iron atom leaves the nanocrystal surface to be coordinated by surrounding chelating agents (here the citrate ions), there are multiple pathways for removing other atoms that will lead to different shapes. Such features suggest a stochastic

process of degradation primarily governed by diffusion of external chelating agents. The large fraction of interfaces as well as the high density of defects originated from the surface curvature may amplify the access of chelating agents to surface iron atoms and thus enhance the iron reactivity.

In this context, we attempted to quantify in which area of the nanocube the onset of degradation takes place. The morphological transformations of nanocubes with the amphiphilic shell begun at {220} planes in 87% of cubes and at {400} planes in 13% (Figure 3A): the edges were more vulnerable to degradation than the faces. To explain such preferential etching, one can put forward thermodynamic considerations, namely, the higher stability of {400} facets, in comparison to {220}.[34] However, the amphiphilic capping around particles also plays a role in particle interactions with surrounding medium. We thus examined the nanocube/shell interface by performing energy-filtered transmission electron microscopy (EFTEM) carbon mapping. Figure 3C displays a direct visualization and quantification of the carbon density around nanoparticles. Noticeably, the coating was not uniformly distributed around nanoparticles. The carbon signal exhibited a 2-fold increase at the interface between two nanocubes in comparison to the free-lying faces of the cubes, suggesting interpenetrated shells of adjacent particles. In some cases, we observe a lack of polymer at the free-lying faces of the nanocube and even more frequently at the edges (Figure 3C,D). Interestingly the regions which were poorly covered by the polymer were also more prone to degradation (see black arrows in Figure 3D). In contrast, a high density organic shell at the angle between two misoriented nanocubes tended to stabilize the coated crystals (see red arrows in Figure 3D). This suggests that the amphiphilic polymers interpenetrated to the surfactant layer from an efficient protective shell against degradation. Conversely, defects in polymer coating generate local reactivity to the acidic chelating medium. In particular, the preferential attack by the {220} planes at the cube edge matches with an uneven polymer coating. This emphasizes the important role of surface curvature in affecting the organization of attached organic molecules and subsequent interactions with surrounding ions. Therefore, initial distribution of the polymer shell likely determines the distribution of degradation onsets.

It is worth emphasizing the differences in degradation kinetics between nanocubes embedded in the amphiphilic polymer shell and those coated with PEG-gallol directly anchored to the iron oxide surface. As observed in Figure 2B, the PEG-coated nanoparticles degrade more rapidly and completely dissolve, while showing no preferential localization for the onset of degradation. While both the amphiphilic polymer and the surfactant layer raise a barrier to the hydrophilic citrate ions, the PEG polymers anchored to discrete sites of the crystal surface could leave more access to the small citrate ions, leading to accelerated degradation. In addition PEG-gallol particles have their isoelectric point close to pH 4. As a consequence, in the pH 4.7 lysosome-like medium, the PEG-gallol could partially dissociate from particles and let the citrates more easily approach and complex the surface iron. Overall, our HRTEM observations highlight that the specific shape of the nanocubes does not prevent their structural degradation. It suggests that the different accessibility of iron chelating agent to the iron oxide crystal, depending on surface functionalization, has a higher impact on the degradation kinetics than the different stability of the particle facets.

Follow-Up of Nanocubes in Suspension in the Lysosome-like Medium. Nanoparticle degradation might contribute to the loss of physical properties necessary for biomedical applications. The magnetic response of iron oxide nanoparticles to external magnetic fields is probed on a statistical assembly of such nanoparticles. Therefore, we examined the evolution of magnetic properties in a suspension of nanoparticles (10 mM iron concentration) exposed to the lysosome-like acidic buffer for a period of 17 days at 37 °C. The concentration of total iron—superparamagnetic iron in the nanocrystal and free iron in ionic forms—was determined by flame spectroscopy for each measurement. Any modifications in nanoparticle magnetism could be interpreted as the signature of their degradation. In line with the observations at the nanometer scale, the evolution of magnetic properties markedly differs depending on the capping agent of the nanocubes (Figure 4).

We observed no clue of degradation for nanocubes coated with the amphiphilic shell: the field-dependent magnetization curve of the nanoparticle suspension, which directly reflects the size distribution of magnetic cores (Supporting Information Figure S5A), was unmodified during this time period. Moreover, the saturation magnetization also remained a constant value around 80 A m^2 kg^{-1}, close to the value of bulk material, showing that the amount of magnetic material did not decrease (Figure 4A). The magneto-thermal properties were also studied in order to estimate the time-dependent potential of nanoparticles for hyperthermia applications. The specific absorption rate (SAR) was measured as a concentration-independent gauge of the heating power of nanoparticles exposed to an alternating magnetic field of 24 kA m^{-1} at a frequency of 520 kHz. At $t = 0$, we found a decrease in SAR of about 33% as soon as nanoparticles with an amphiphilic shell were transferred from water to the acidic buffer medium. However, over the 17 days in acidic medium, the SAR remained unchanged (Figure 4D and Supporting Information Figure S5B). To explain such unexpected stability of magnetic properties in the lysosome-like medium, we hypothesize that its acidic

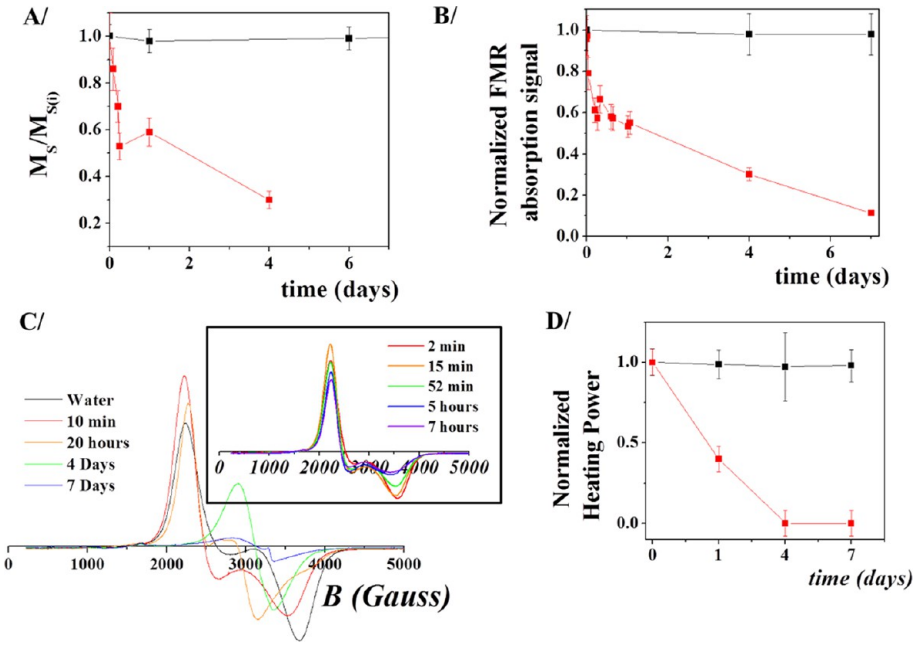

Figure 4. Magnetic follow-up of the nanocube degradation in the lysosome-like medium. Evolution of the saturation magnetization (normalized to its initial value) (A) and ferromagnetic resonance absorption signal (B) over time collected at 310 K in a suspension of nanoparticles (PEG-coated in red, amphiphilic polymer-coated in black) dispersed in the lysosome-like medium. Note that the free iron species which lack ferromagnetic order do not contribute to the FMR signal at room temperature. (C) Ferromagnetic resonance spectrum of PEG-coated nanocubes (2 μL, 10 mM iron) for different times in the lysosome-like medium. Note the transformation of the highly asymmetric FMR spectrum of initial nanocubes into a symmetric one shifted toward higher field. (D) Normalized heating power (specific absorption rate normalized to its initial value at $t = 0$) as a function of incubation time in the acidic buffer using a magnetic field amplitude of 24 kA m^{-1} at a frequency of 520 kHz.

nature could cause the destabilization of the suspension and the formation of aggregates, which become resistant to degradation. This assumption was sustained by dynamic light scattering (DLS) measurements (Supporting Information Figure S6): the hydrodynamic radius of the nanoparticles was 37 nm in water and increased to the micrometer range within minutes in the acidic medium. No further evolution of the hydrodynamic size was observed in the degradation buffer. In the meantime, the SAR and ferromagnetic resonance (FMR) spectrum (Supporting Information Figures S5B and S7), some properties that are sensitive to particle clustering through the enhancement of interparticle dipolar interactions were rapidly modified in the acidic medium compared to water. However, the remarkable persistence of magnetic properties over extended time in acidic medium likely reflects the robustness of shell-protected aggregates against degradation, in line with the above TEM observations on three-dimensional aggregates of nanocubes (Figure 2F).

In contrast, the PEG-coated nanocubes exhibited a contrasted behavior. Their magnetization decreased over time, representing less than 30% of the initial value after 4 days in the lysosome-like medium (Figure 4A). Consistently, the total absorption signal (Figure 4B) of their ferromagnetic resonance spectrum diminished on time, reflecting the loss of ferromagnetic nanomaterials (Figure 4B,C). Moreover, the asymmetric FMR spectrum of the initial nanocubes was being transformed into a symmetric one, progressively shifted toward higher field, which is characteristic of polydisperse spherical nanoparticles.[35] This evolution, supported by the TEM images over time (Supporting Information Figure S8), is the macroscopic signature of shape and size transformation upon degradation. We note that this evolution is highlighted by using cubes as initial shape, in contrast to the spheres, which tend to conserve their shape upon degradation.[18] Meanwhile, the SAR continuously decreased over time. We note that a transient particle aggregation could be observed in the first hours in acidic medium (Supporting Information Figure S9), but the suspension remained stable afterward, while dissolution of nanoparticles went on.

While the macroscopic follow-up overall is in accordance with nanoscale monitoring on the TEM grid, it is worth mentioning the longer time scale of nanoparticle transformation in suspension. Accelerated degradability of nanoparticles observed on the carbon film is likely due to the higher ratio of available chelating agent with respect to the number of particles. This is also supported by previous findings on 7−8 nm maghemite nanoparticles showing that the degradation rate was dependent on the citrate over iron concentration ratio.[18] Here, we have evidenced that both citrate availability and accessibility for the iron surface (depending on the capping agents) play critical roles on nanoparticle degradability. Our results suggest that the crystal morphology and thermodynamic considerations may not be the

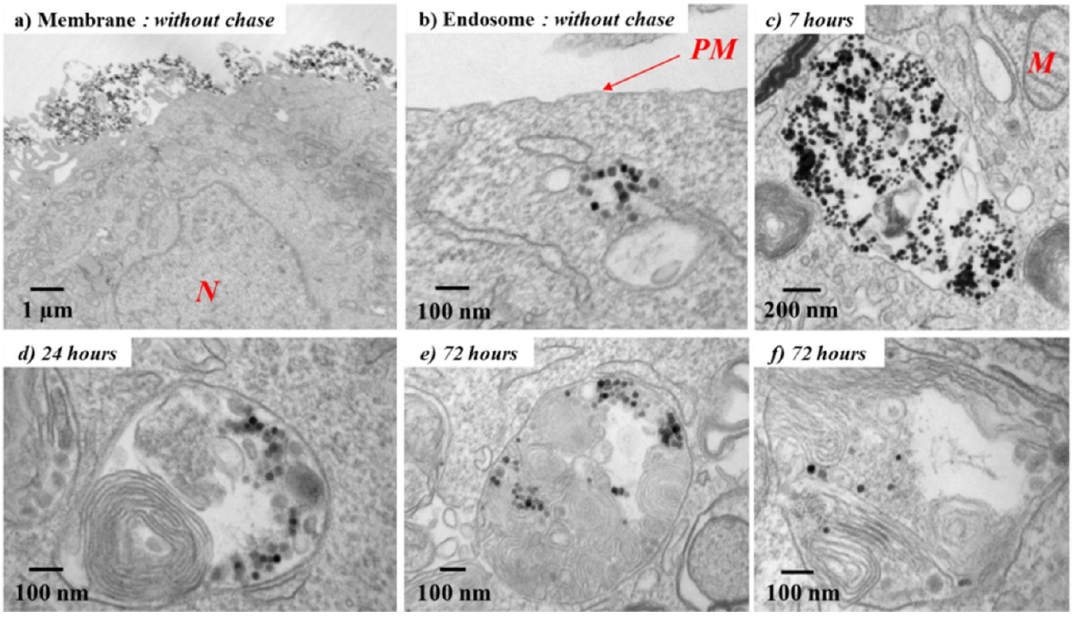

Figure 5. TEM micrographs of PC3 tumor cells incubated at 37 °C with a suspension of nanocubes coated with amphiphilic polymers (0.5 mM in iron) for 1 h and cultured for different chase periods. (a) After the incubation (without chase), the nanocubes are still present on the plasma membrane or (b) already internalized into early endosomes with a clear background. (c) On increasing the chase period, nanocubes are confined in endosomes in aggregated form, then (d) localize within heterolysosomes, which are electron dense and are characterized by numerous multilamellar bodies and high density proteins. (e,f) Nanoparticles appear more and more dispersed within lysosomes and therefore start degrading (N, nucleus; M, mitochondria; PM, plasma membrane).

prominent factors governing surface reactivity at least at the first stage of degradation. The 7−8 nm maghemite nanospheres embedded in dextran showed comparable kinetics of degradation as the PEG-coated 21 nm nanocubes.[18] In contrast, the same nanospheres coated with a derivative of glucose were more resistant to degradation, likely due to the strong phosphonate anchorage of these ligands on the iron surface.

In our study, the cube edges influence the distribution of polymers on the crystal and therefore the place of degradation onset. However, a comprehensive comparison of cubes and spheres with equivalent volume would be needed to unravel the role of morphology and size on surface reactivity.

Follow-Up of Nanocubes in Cultured Cells. The lysosome-like medium used above comprises minimal components that actually enter into account in the real intracellular environment. However, cellular processing of nanoparticles is a dynamical active process primarily orchestrated by endocytic machinery, a complex array of vesicles and proteins. SKOV3 ovarian and PC3 prostatic carcinoma cells were chosen to assess the processing of nanocubes in the first 72 h following internalization. These cellular models are of practical interest to investigate biotransformation of nanocubes used for treatment of solid tumors by magnetically induced hyperthermia. Nanocubes with amphiphilic shells were incubated with the two cancer cell lines at a concentration of 0.5 mM in iron for 1 h at 37 °C. For PC3 cells, a kinetic study was conducted according to the chase duration, ranging from 0 min to 72 h (Figure 5). Without chase, the nanoparticles were first adsorbed on cell plasma membrane (Figure 5a). Subsequently, the early budding of transport vesicles from plasma membrane (Figure 5b), the fusion of early endosomes with late endosomes, and their ensuing fusion with lysosomes direct redistribution of nanoparticles and specify their localization and fate within the cell.[36,37] In the first hours, aggregates of nanocubes were observed in endosomes with a clear background (Figure 5c). At longer time points, the nanoparticles became less aggregated within larger compartments, presumably lysosomes or heterolysosomes, which appeared more contrasted due to high protein content and numerous intravesicular membranes (Figure 5d,e, and f). For the other type of cancer cells, the SKOV3 ovarian cells, the study focuses on a chase of 7 h. As for the PC3 cells, nanoparticles were aggregated in endosomes or more dispersed in denser lysosomal compartments (Supporting Information Figure S10). For both cell lines, some particles with eroded shapes and diminished sizes were found dispersed within electron-dense areas (Figure 5d,e, and f and Supporting Information Figure S10). The apparent segregation of nanoparticles into membrane- and protein-rich regions suggests that their transformation occurs in these regions.

Follow-Up of Nanocubes in Murine Livers and Spleens. Observations of long-term biotransformation in mice confirmed the role of intracellular nanoparticle distribution in their bioavailability and assimilation. The PEG-coated nanocubes were injected intravenously to mice at a dose of 50 μmol iron/kg of body weight (the usual dose for preclinical MRI study), and *ex vivo*

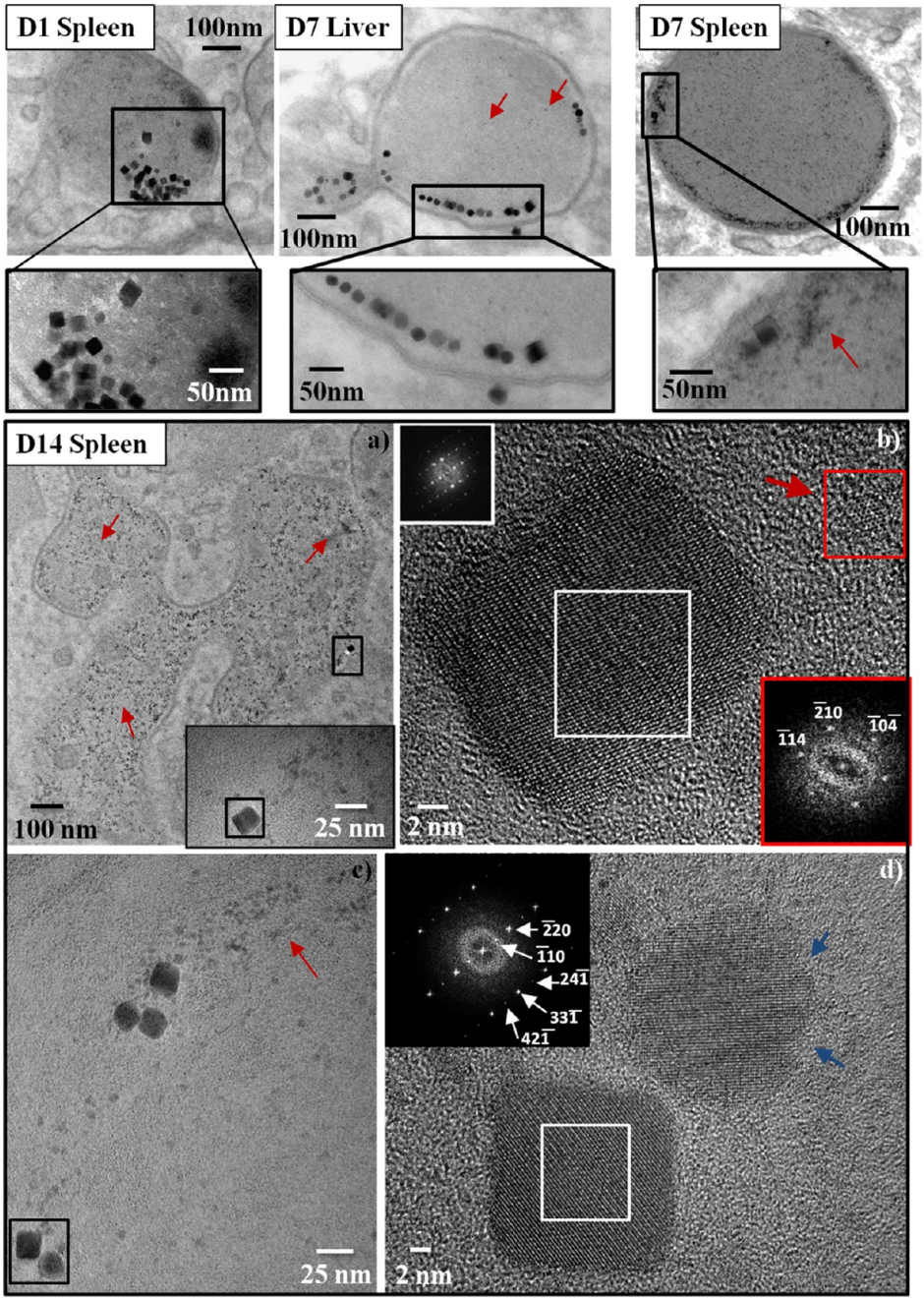

Figure 6. Intracellular degradation of PEG-coated nanocubes in murine liver and spleen after intravenous injection. The intravesicular spatial distribution of nanoparticles evolves over time: early after injection (day 1), dense assemblies of nanocubes avoid the cell from particle degradation and release of cytotoxic free iron. At longer times (days 7 and 14), the nanoparticles are transferred into protein-rich lysosomes in which they are more dispersed and susceptible to degradation. Red arrows show the coexistence of monodisperse iron-rich ferritin protein of 5.3 ± 0.8 nm diameter with some degraded or resilient nanocubes, suggesting a protein-triggered degradation and local iron transfer. High-resolution imaging performed 14 days after injection shows that degraded and resilient nanocubes maintain their initial structure (the spinel inverse and the vacancy-ordered γ-Fe_2O_3 structures along the [103] and [116] zones axes on the images (b) and (d), respectively. The blue arrows highlight the rough surfaces of the degraded nanostructures. The Fourier transform of the atomic structure of the ferritin core in image b (D14 spleen, red squares) shows unambiguously a hematite structure oriented along the [48−1] zone axis.

TEM analysis at different time points was focused on liver and spleen as blood-injected nanoparticles are mostly taken up by macrophages on these organs (Supporting Information Figures S11−S13).[15,17,20] One day post-injection, nanocubes were mostly aggregated within endosomes or more contrasted lysosomes (Figure 6), in line with our findings on cultured cells. Segregation into protein-rich regions was observed, as well. At days 7 and 14 post-injection, nanocubes were scarcer and more dispersed and mainly observed on the periphery of lysosomes. Remarkably, we note that the presence of smaller monodisperse electron-dense

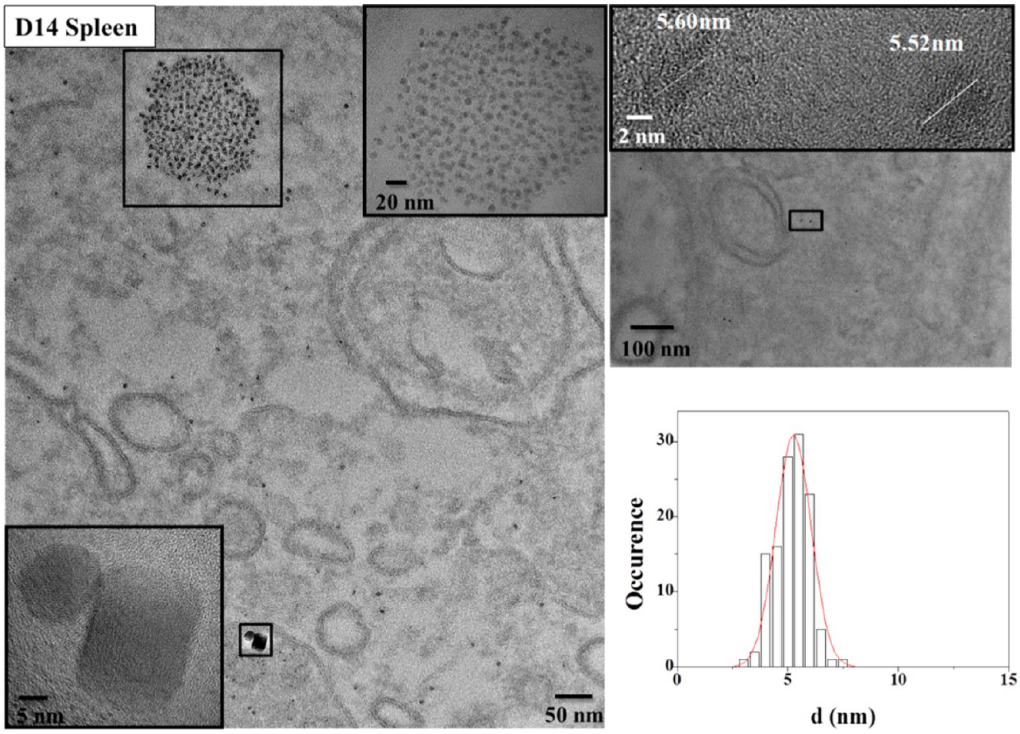

Figure 7. Enrichment in iron-filled ferritin proteins in the cytoplasm close to lysosomes containing residual nanocubes in mouse spleen at day 14 post-injection. Spherical iron-rich proteins are either dispersed in the cytoplasm or form large assemblies (top left). Here, on the HRTEM image, they exhibit poorly crystalline internal structure (top right). Their size distribution deduced from TEM images follows a Gaussian distribution with a mean size equal to 5.3 ± 0.8 nm. The size histogram was determined using micrographs at magnification of ×50K on about 150 nanoparticles.

spherical nanoparticles of 4−7 nm in diameter either dispersed or gathered to form electron-dense conglomerates, which coexist with the residual cubes (Figure 6, Figure 7, and Supporting Information Figure S13). Energy-dispersive X-ray spectrometry (EDX) and HRTEM analysis performed on ultrafine (30 nm) organ slices confirmed that these intracellular monodisperse nano-objects contain iron and show poorly crystalline or crystalline arrangements, such as the iron oxide hematite structure (Figures 6b, 7, and Supporting Information Figure S13), that are different from the spinel inverse or the vacancy-ordered γ-Fe_2O_3 structures observed in residual nanocubes. The features of these intracellular objects are characteristic for iron-filled ferritin proteins, which are ubiquitous proteins storing iron in polyphasic and nontoxic forms.[16,17,38,39]

As iron is both vital and potentially toxic for human health, a highly regulated interacting network is responsible for iron homeostasis.[40] The transit pool of iron in the cytosol is presumably bound to low molecular weight chelates, such as citrate, ATP, or pyrophosphate, and contributes to iron-mediated toxicity as a source of redox-active iron.[41] Therefore, the excess iron, in its free ferrous form Fe(II), is oxidized and then sequestered into ferritin proteins. Iron regulatory proteins are able to sense the cytosolic iron concentration and coordinate the regulation of both iron export (mainly by transferrin) and iron storage by ferritin.

Here, we show that exogenous iron oxide nanocubes are sequestered first in endosomes and ultimately in lysosomes. The shell surrounding intracellular nanocubes is likely different from the initial one and may also vary due to multiple interactions with proteins encountered on the nanoparticle's journey from blood to intracellular compartments.[10,12] As long as nanoparticles remain intact, they are not a source of potentially toxic free iron. Nanoparticle dissolution requires the availability of chelating agents, which should also be capable of accessing the nanoparticle core. We observe here the close proximity of iron-rich ferritin with degraded nanocubes. The shape and the rough surfaces of these degraded structures closely resemble those observed *in situ* during tracking single-particle transformation (Figure 6). These observations suggest a local transformation pathway allowing the transfer and recycling of iron from the iron oxide nanocrystals to the ferritin protein nanocavities. Such a putative mechanism of degradation and transfer would need both time and spatial regulation of chelators and reductants produced intracellularly. Moreover, the availability of iron chelators to the nanocube surface could be favored by their reorganization and segregation in the lysosome. Likewise, the degradation process of nanoparticles could be contingent to the production of ferritin proteins, able to store the excess iron, which in turn could regulate the degradation rate. We have shown that iron dissolution

and transfer results in residual eroded particle shapes which conserve their crystalline structure. However, the way ferritin can mineralize iron species coming from other nanocrystals and the intermediates involved to traverse the gated protein pores are unknown. The prominent role of ferritin in recycling nanoparticulate iron could be supported by the recent view of ferritin as a biomineralization reactor: catalytic sites and gated pores in the flexible and dynamic protein cage should control in and out flow of iron.[42,43]

Altogether, our *in vivo* observations at the atomic scale suggest a nanodegradation pathway controlled by surface reactivity, intracellular nanoparticle distribution, and availability of iron chelators and emphasize the determinant role of iron storage proteins in the subsequent sequestration of free iron released by exogenous nanocubes. The proposed mechanism of long-term *in vivo* transformation, which transfers iron from a safe form in the initial nanoparticles to another nontoxic form in ferritin, could explain the excellent tolerance profile reported so far for smaller spherical iron oxide nanoparticles at clinical dose (10−50 μmol iron/kg).[15,20,44] It must be noted, however, that the kinetics of iron oxide biotransformation and catabolism *in vivo* may depend on several factors, such as the dose injected (which may be up to 3−50-fold higher in order to induce therapeutic hyperthermia), the route of administration, the considered organ, and the mechanisms of nanoparticle (and iron) translocation between organs. A comprehensive investigation of nanoparticle fate *in vivo* requires a specific quantitative follow-up by nanometrology methods. For example, preliminary FMR quantification of the amount of nanocubes which conserve their superparamagnetic properties shows that the biodegradation takes more time in the spleen than in the liver (−93% *versus* −69% at day 30 compared to day 1, respectively). The higher concentration of nanocubes in the spleen compared to the liver (1.3-fold) could partly account for these kinetics, considering that the degradation requires the availability of enough storage proteins. Therefore, one can envision some transient or even lasting saturation of the physiological iron homeostasis when a high dose of nanoparticles is injected, which could lead to a long-term persistence of the nanoparticles. In addition, although this aspect has been somehow ignored so far, the degradability of nanoparticles and subsequent loss of their magnetic properties should be thoroughly investigated in the conditions used for MRI diagnostic or hyperthermic tumor treatment. Intracellular transformation of nanoparticles is likely to alter their magnetic properties and diminish their efficiency as MRI contrast agents or heating sources. However, considering that the very local environment and the distribution of nanoparticles should drive their reactivity, it is necessary to monitor their degradability *in situ* in the relevant context (*e.g.*, tumor microenvironment) before drawing conclusions.

CONCLUSION

Although the molecular mechanism of iron transfer is not elucidated here, we have evidenced, for the first time, some key processes governing the fate of nanoparticles in a biological environment. The monitoring of single-particle degradation at atomic scale revealed a stochastic corrosion process, whose sites of onset depend on the nature and the distribution of particle coating. The organization of nanoparticles plays a critical role for their transformation by the environment which has been demonstrated both *in vitro* and *in vivo*. In this regard, aggregation tends to protect from degradation while segregation is favorable to iron release from nanocrystals. The availability of chelating agents and their accessibility to the nanoparticle core are the key factors regulating degradation kinetics. We hypothesize that cells could timely orchestrate the redistribution of a nanoparticle from a dense assembly in early endosomes to a more dispersed and exposed state into lysosomal compartments. This mechanism might be activated in order to retard the release of free cytotoxic iron ions, only in lysosome where ferritin proteins can store the released iron in a safe form. The *in situ* monitoring of nanoparticle transformation at the nanoscale, as reported here, might be easily applicable to other nanomaterials to provide critical insight about their fate in the organism.

MATERIALS AND METHODS

Nanoparticles. Nanoparticles were prepared and characterized as described previously (see Supporting Information S1 for details).[21,45]

Lysosome-like Buffer Solution. Degradation experiments were performed in 20 mM citric acid at pH 4.7. The citrate buffer was prepared by mixing 4.4 mM of citric acid ($C_6H_8O_7$, Fluka, >99.5%) and 5.6 mM of sodium citrate tribasic ($C_6H_5Na_3O_7 \cdot 2H_2O$, Fluka, >99%) in 500 mL of purified water.

Aberration-Corrected High-Resolution Transmission Electron Microscopy (HRTEM). Combining high-resolution and energy-filtered transmission electron microscopy is a method of choice to characterize the atomic structure of hybrid nanosystems made of an inorganic nanoparticle and a shell of soft materials. These TEM investigations were performed with the newly developed JEOL ARM 200 F microscope operating at 200 kV. This microscope is equipped together with a CEOS aberration corrector, a cold field emission gun, and a Gatan GIF quantum ER.[46,47] Lacey carbon TEM grids (agar) were used to follow the degradation mechanisms by HRTEM. EFTEM experiments were performed on nanocubes distributed on an amorphous silicon-coated TEM grid (SIMPore), in order to visualize the distribution of carbon-rich polymer on the nanoparticle surface.[48] Carbon maps were calculated by using the three window technique on the carbon K-edge at 284 eV.

Magnetic Measurements. Magnetization measurements were carried out on a Quantum Design MPMS-5S SQUID magnetometer.

Field-dependent magnetization curves were measured at 310 K as function of the external field in the range of 0 to 3×10^4 Gauss. Ferromagnetic resonance (FMR) spectra were acquired at room temperature, using a Varian E102 EPR spectrometer operating at 9.25 GHz, for nanoparticles (2 μL) dispersed in water or in the lysosome-like medium at different incubation times (microwave power 1 mW, modulation field 10 G). Ferromagnetic absorption signal was obtained by double integration of the resonance spectrum.

Specific Absorption Rate Measurement. Hyperthermia tests were performed on 300 μL of sample using a homemade device.[49] A fluoro-optic thermometer fiber probe (Luxtron Corp., CA) was used to probe the temperature every 0.7 s. By circulating nonane into the coil, the temperature inside the sample holder was kept to 37 °C. Experiments were carried out by using an applied field of 24 kA m^{-1} and a frequency of 520 kHz. The specific absorption rate (SAR) of nanoparticles was determined according to $SAR = (1/m_e)(\Sigma_i c_i m_i (dT/dt))$, where m_e is the total mass of iron, c_i and m_i are the specific heat and the mass of the different species in solution (in this specific case, we considered only water), and dT/dt is the initial slope of the time-dependent temperature increase $T(t)$. All reported SAR values and error bars were calculated from the mean and standard deviation of at least four experimental measurements. SAR measurements for different incubation time in the lysosome-like medium were performed on independent suspension for each time point.

Dynamic Light Scattering Measurements. Dynamic light scattering (DLS) measurements were performed on a Zeta Sizer Nano ZS (Malvern Instruments) equipped with a 5.0 mW He−Ne laser operating at 633 nm and an Avalanche photodiode detector.

Cell Culture, Magnetic Labeling, and Preparation for TEM Analysis. Cells were maintained as monolayer cultures in Dulbecco's modified Eagle medium (DMEM) supplemented with 10% fetal bovine serum, 1% penicillin-streptomycin at 37 °C and 5% of CO_2. For cell labeling, the incubation medium was prepared by adding a filter-sterilized suspension of magnetic nanoparticles in serum-free Roswell Park Memorial Institute medium (RPMI-1640 medium) supplemented with 5 mM of citrate to obtain an iron concentration of [Fe] = 0.5 mM. Cells were incubated with this medium for 1 h at 37 °C. Then the cells were rinsed three times with RPMI medium and immediately processed for electron microscopy ("without chase" condition) or cultured in complete DMEM medium for different chase periods (7, 24, and 72 h). At the end of the chase period, cells were trypsinized, centrifuged at 1200 rpm for 5 min, and prepared for electron microscopy. Cells were washed three times in 0.1 M cacodylate buffer and fixed with 2.5% glutaraldehyde in cacodylate buffer at 4 °C for 30 min. Cells were then postfixed with osmium tetraoxide 1% and passed through uranyl acetate. Samples were then dehydrated in an ethanol series (30−100%) and embedded in epoxy medium (EPON 812; Shell Chemical, San Francisco, CA). Thin sections (70 nm) were collected onto 200 mesh cooper grids and counterstained with lead citrate before examination with Zeiss EM902 electron microscope operated at 80 kV (MIMA2- UR1196 Génomique et Physiologie de la Lactation, INRA, Plateau de Microscopie Electronique 78352, Jouy en Josas, France).

***In Vivo* Study.** Animal experiments were conducted in line with French Agriculture Ministry guidelines. Nine 8 week old C57/Bl6 mice (mean weight 20.5 ± 1 g) (Janvier, France) were injected in the recto-orbital vein of polyethylene glycol-coated nanocubes in 100 μL of physiological saline medium at a dose of 50 μmol/kg. Two C57/Bl6 mice served as noninjected controls. Three nanoparticle-injected mice were sacrificed at each time point after nanoparticle injection (days D1, D7, D14), and two controls were sacrificed at the end of the study. Livers and spleens were excised and prepared for TEM characterizations.

TEM of Organs. Organs were cut into 1 mm^3 pieces after excision and fixed with 2% glutaraldehyde in 0.1 M sodium cacodylate buffer, postfixed with 1% osmium tetroxide containing 1.5% potassium cyanoferrate, gradually dehydrated in ethanol, and embedded in Epon. Thin sections (70 nm) of selected zones were observed with Zeiss EM902 electron microscope operated at 80 kVe (MIMA2- UR1196 Génomique et Physiologie de la Lactation, INRA, Plateau de Microscopie Electronique 78352, Jouy en Josas, France). Ultrathin sections (30 nm) were specially prepared for high-resolution imaging and EDX analysis, performed on the aberration-corrected JEOL ARM 200F operating at 80 kV.

Conflict of Interest: The authors declare no competing financial interest.

Acknowledgment. We are grateful to Region Ile-de-France for convention SESAME E1845, for the support of the JEOL ARM 200F electron microscope recently installed at the Paris Diderot University. This work was supported by the European Project Magnifyco (Contract NMP4-SL-2009-228622) and ENCITE (JK) (European Network for Cell Imaging and Tracking Expertise, Grant Agreement Number 201842). We thank Jacques Servais for hyperthermia setup, Riccardo Di Corato for help with the nanoparticle preparation, Sophie Chat for TEM of organs and cells, Aude Michel for iron assay, Florent Carn for DLS measurements, François Gendron for magnetic measurements, and Nathalie Luciani, Jean-Claude Bacri, and Christian Ricolleau for fruitful discussion.

Supporting Information Available: Synthetic procedure and complementary details on nanocubes degradation *in vitro* and *in vivo* (Figures S1−S13). This material is available free of charge *via* the Internet at http://pubs.acs.org.

REFERENCES AND NOTES

1. Lowry, G. V.; Gregory, K. B.; Apte, S. C.; Lead, J. R. Transformations of Nanomaterials in the Environment. *Environ. Sci. Technol.* **2012**, *46*, 6893–6899.
2. Thomas, C. R.; George, S.; Horst, A. M.; Ji, Z.; Miller, R. J.; Peralta-Videa, J. R.; Xia, T.; Pokhrel, S.; Mädler, L.; Gardea-Torresdey, J. L.; *et al.* Nanomaterials in the Environment: From Materials to High-Throughput Screening to Organisms. *ACS Nano* **2011**, *5*, 13–20.
3. Rivera-Gil, P.; De Koker, S.; De Geest, B. G.; Parak, W. J. Intracellular Processing of Proteins Mediated by Biodegradable Polyelectrolyte Capsules. *Nano Lett.* **2009**, *9*, 4398–4402.
4. Zhou, X.; Andoy, N. M.; Liu, G.; Choudhary, E.; Han, K.-S.; Shen, H.; Chen, P. Quantitative Super-resolution Imaging Uncovers Reactivity Patterns on Single Nanocatalysts. *Nat. Nanotechnol.* **2012**, *7*, 237–241.
5. Levard, C.; Hotze, E. M.; Lowry, G. V.; Brown, G. E. Environmental Transformations of Silver Nanoparticles: Impact on Stability and Toxicity. *Environ. Sci. Technol.* **2012**, *46*, 6900–6914.
6. Xia, T.; Zhao, Y.; Sager, T.; George, S.; Pokhrel, S.; Li, N.; Schoenfeld, D.; Meng, H.; Lin, S.; Wang, X.; *et al.* Decreased Dissolution of ZnO by Iron Doping Yields Nanoparticles with Reduced Toxicity in the Rodent Lung and Zebrafish Embryos. *ACS Nano* **2011**, *5*, 1223–1235.
7. George, S.; Lin, S.; Ji, Z.; Thomas, C. R.; Li, L.; Mecklenburg, M.; Meng, H.; Wang, X.; Zhang, H.; Xia, T.; *et al.* Surface Defects on Plate-Shaped Silver Nanoparticles Contribute to Its Hazard Potential in a Fish Gill Cell Line and Zebrafish Embryos. *ACS Nano* **2012**, *6*, 3745–3759.
8. Cedervall, T.; Lynch, I.; Lindman, S.; Berggard, T.; Thulin, E.; Nilsson, H.; Dawson, K. A.; Linse, S. Understanding the Nanoparticle-Protein Corona Using Methods To Quantify Exchange Rates and Affinities of Proteins for Nanoparticles. *Proc. Natl. Acad. Sci. U.S.A.* **2007**, *104*, 2050–2055.
9. Casals, E.; Pfaller, T.; Duschl, A.; Oostingh, G. J.; Puntes, V. Time Evolution of the Nanoparticle Protein Corona. *ACS Nano* **2010**, *4*, 3623–3632.
10. Lundqvist, M.; Stigler, J.; Cedervall, T.; Berggard, T.; Flanagan, M. B.; Lynch, I.; Elia, G.; Dawson, K. The Evolution of the Protein Corona Around Nanoparticles: A Test Study. *ACS Nano* **2011**, *5*, 7503–7509.
11. Dobrovolskaia, M. A.; Aggarwal, P.; Hall, J. B.; McNeil, S. E. Preclinical Studies To Understand Nanoparticle Inter action with the Immune System and Its Potential Effects on Nanoparticle Biodistribution. *Mol. Pharmaceutics* **2008**, *5*, 487–495.

12. Lartigue, L.; Wilhelm, C.; Servais, J.; Factor, C.; Dencausse, A.; Bacri, J.-C.; Luciani, N.; Gazeau, F. Nanomagnetic Sensing of Blood Plasma Protein Interactions with Iron Oxide Nanoparticles: Impact on Macrophage Uptake. *ACS Nano* **2012**, *6*, 2665–2678.
13. Fayol, D.; Luciani, N.; Lartigue, L.; Gazeau, F.; Wilhelm, C. Managing Magnetic Nanoparticle Aggregation and Cellular Uptake: A Precondition for Efficient Stem-Cell Differentiation and MRI Tracking. *Adv. Healthcare Mater.* **2012**, *2*, 313–325.
14. Ohkuma, S.; Poole, B. Fluorescence Probe Measurement of the Intralysosomal pH in Living Cells and the Perturbation of pH by Various Agents. *Proc. Natl. Acad. Sci. U.S.A.* **1978**, *75*, 3327–3331.
15. Weissleder, R.; Stark, D. D.; Engelstad, B. L.; Bacon, B. R.; Compton, C. C.; White, D. L.; Jacobs, P.; Lewis, J. Superparamagnetic Iron Oxide: Pharmacokinetics and Toxicity. *AJR Am. J. Roentgenol.* **1989**, *152*, 167–173.
16. Arbab, A. S.; Wilson, L. B.; Ashari, P.; Jordan, E. K.; Lewis, B. K.; Frank, J. A. A Model of Lysosomal Metabolism of Dextran Coated Superparamagnetic Iron Oxide (SPIO) Nanoparticles: Implications for Cellular Magnetic Resonance Imaging. *NMR Biomed.* **2005**, *18*, 383–389.
17. Okon, E.; Pouliquen, D.; Okon, P.; Kovaleva, Z. V.; Stepanova, T. P.; Lavit, S. G.; Kudryavtsev, B. N.; Jallet, P. Biodegradation of Magnetite Dextran Nanoparticles in the Rat. A Histologic and Biophysical Study. *Lab. Invest.* **1994**, *71*, 895–903.
18. Levy, M.; Lagarde, F.; Maraloiu, V. A.; Blanchin, M. G.; Gendron, F.; Wilhelm, C.; Gazeau, F. Degradability of Superparamagnetic Nanoparticles in a Model of Intracellular Environment: Follow-up of Magnetic, Structural and Chemical Properties. *Nanotechnology* **2010**, *21*, 395103–395200.
19. Levy, M.; Wilhelm, C.; Luciani, N.; Devaux, V.; Gendron, F.; Luciani, A.; Devaud, M.; Gazeau, F. Nanomagnetism Reveals the Intracellular Clustering of Nanoparticles in the Organism. *Nanoscale* **2011**, *3*, 4402–4410.
20. Levy, M.; Luciani, N.; Alloyeau, D.; Elgrabli, D.; Deveaux, V.; Pechoux, C.; Chat, S.; Wang, G.; Vats, N.; Gendron, F.; *et al.* Long Term *In Vivo* Biotransformation of Iron Oxide nanoparticles. *Biomaterials* **2011**, *32*, 3988–3999.
21. Guardia, P.; Di Corato, R.; Lartigue, L.; Wilhelm, C.; Espinosa, A.; Garcia-Hernandez, M.; Gazeau, F.; Manna, L.; Pellegrino, T. Water-Soluble Iron Oxide Nanocubes with High Values of Specific Absorption Rate for Cancer Cell Hyperthermia Treatment. *ACS Nano* **2012**, *6*, 3080–3091.
22. Bae, K. H.; Park, M.; Do, M. J.; Lee, N.; Ryu, J. H.; Kim, G. W.; Kim, C.; Park, T. G.; Hyeon, T. Chitosan Oligosaccharide-Stabilized Ferrimagnetic Iron Oxide Nanocubes for Magnetically Modulated Cancer Hyperthermia. *ACS Nano* **2012**, *6*, 5266–5273.
23. Noh, S.-h.; Na, W.; Jang, J.-t.; Lee, J.-H.; Lee, E. J.; Moon, S. H.; Lim, Y.; Shin, J.-S.; Cheon, J. Nanoscale Magnetism Control *via* Surface and Exchange Anisotropy for Optimized Ferrimagnetic Hysteresis. *Nano Lett.* **2012**, *12*, 3716–3721.
24. Lee, N.; Choi, Y.; Lee, Y.; Park, M.; Moon, W. K.; Choi, S. H.; Hyeon, T. Water-Dispersible Ferrimagnetic Iron Oxide Nanocubes with Extremely High r_2 Relaxivity for Highly Sensitive *In Vivo* MRI of Tumors. *Nano Lett.* **2012**, *12*, 3127–3131.
25. Lee, N.; Kim, H.; Choi, S. H.; Park, M.; Kim, D.; Kim, H.-C.; Choi, Y.; Lin, S.; Kim, B. H.; Jung, H. S.; *et al.* Magnetosome-like Ferrimagnetic Iron Oxide Nanocubes for Highly Sensitive MRI of Single Cells and Transplanted Pancreatic Islets. *Proc. Natl. Acad. Sci. U.S.A.* **2011**, *108*, 2662–2667.
26. Guardia, P.; Pérez, N. S.; Labarta, A.; Batlle, X. Controlled Synthesis of Iron Oxide Nanoparticles over a Wide Size Range. *Langmuir* **2010**, *26*, 5843–5847.
27. Kovalenko, M. V.; Bodnarchuk, M. I.; Lechner, R. T.; Hesser, G.; Schäffler, F.; Heiss, W. Fatty Acid Salts as Stabilizers in Size- and Shape-Controlled Nanocrystal Synthesis: The Case of Inverse Spinel Iron Oxide. *J. Am. Chem. Soc.* **2007**, *129*, 6352–6353.
28. Wang, Z. L. Transmission Electron Microscopy of Shape-Controlled Nanocrystals and Their Assemblies. *J. Phys. Chem. B* **2000**, *104*, 1153–1175.
29. Van Oosterhout, G. W.; Rooijmans, C. J. M. A New Superstructure in Gamma-Ferric Oxide. *Nature* **1958**, *181*, 44.
30. Pellegrino, T.; Manna, L.; Kudera, S.; Liedl, T.; Koktysh, D.; Rogach, A. L.; Keller, S.; Rädler, J.; Natile, G.; Parak, W. J. Hydrophobic Nanocrystals Coated with an Amphiphilic Polymer Shell: A General Route to Water Soluble Nanocrystals. *Nano Lett.* **2004**, *4*, 703–707.
31. Di Corato, R.; Quarta, A.; Piacenza, P.; Ragusa, A.; Figuerola, A.; Buonsanti, R.; Cingolani, R.; Manna, L.; Pellegrino, T. Water Solubilization of Hydrophobic Nanocrystals by Means of Poly(maleic anhydride-*alt*-1-octadecene). *J. Mater. Chem.* **2008**, *18*, 1991–1996.
32. Amstad, E.; Zurcher, S.; Mashaghi, A.; Wong, J. Y.; Textor, M.; Reimhult, E. Surface Functionalization of Single Superparamagnetic Iron Oxide Nanoparticles for Targeted Magnetic Resonance Imaging. *Small* **2009**, *5*, 1334–1342.
33. Gabizon, A.; Shmeeda, H.; Barenholz, Y. Pharmacokinetics of PEGylated Liposomal Doxorubicin: Review of Animal and Human Studies. *Clin. Pharmacokinet.* **2003**, *42*, 419–436.
34. Tao, A. R.; Habas, S.; Yang, P. Shape Control of Colloidal Metal Nanocrystals. *Small* **2008**, *4*, 310–325.
35. Gazeau, F.; Shilov, V.; Bacri, J.-C.; Dubois, E.; Gendron, F.; Perzynski, R.; Raikher, Y. L.; Stepanov, V. I. Magnetic Resonance of Nanoparticles in a Ferrofluid: Evidence of Thermofluctuational Effects. *J. Magn. Magn. Mater.* **1999**, *202*, 535–546.
36. Schulze, E.; Ferrucci, J. T., Jr.; Poss, K.; Lapointe, L.; Bogdanova, A.; Weissleder, R. Cellular Uptake and Trafficking of a Prototypical Magnetic Iron Oxide Label *in Vitro*. *Invest. Radiol.* **1995**, *30*, 604–610.
37. Loubery, S.; Wilhelm, C.; Hurbain, I.; Neveu, S.; Louvard, D.; Coudrier, E. Different Microtubule Motors Move Early and Late Endocytic Compartments. *Traffic* **2008**, *9*, 492–509.
38. Gálvez, N.; Fernández, B.; Sánchez, P.; Cuesta, R.; Ceolín, M.; Clemente-León, M.; Trasobares, S.; López-Haro, M.; Calvino, J. J.; Stéphan, O.; *et al.* Comparative Structural and Chemical Studies of Ferritin Cores with Gradual Removal of Their Iron Contents. *J. Am. Chem. Soc.* **2008**, *130*, 8062–8068.
39. Quintana, C.; Cowley, J. M.; Marhic, C. Electron Nanodiffraction and High-Resolution Electron Microscopy Studies of the Structure and Composition of Physiological and Pathological Ferritin. *J. Struct. Biol.* **2004**, *147*, 166–178.
40. Hower, V.; Mendes, P.; Torti, F. M.; Laubenbacher, R.; Akman, S.; Shulaev, V.; Torti, S. V. A General Map of Iron Metabolism and Tissue-Specific Subnetworks. *Mol. BioSyst.* **2009**, *5*, 422–443.
41. Papanikolaou, G.; Pantopoulos, K. Iron Metabolism and Toxicity. *Toxicol. Appl. Pharmacol.* **2005**, *202*, 199–211.
42. Liu, X.; Theil, E. C. Ferritins: Dynamic Management of Biological Iron and Oxygen Chemistry. *Acc. Chem. Res.* **2005**, *38*, 167–175.
43. Theil, E. C. Ferritin Protein Nanocages Use Ion Channels, Catalytic Sites, and Nucleation Channels To Manage Iron/Oxygen Chemistry. *Curr. Opin. Chem. Biol.* **2011**, *15*, 304–311.
44. Kedziorek, D. A.; Muja, N.; Walczak, P.; Ruiz-Cabello, J.; Gilad, A. A.; Jie, C. C.; Bulte, J. W. M. Gene Expression Profiling Reveals Early Cellular Responses to Intracellular Magnetic Labeling with Superparamagnetic Iron Oxide Nanoparticles. *Magn. Reson. Med.* **2010**, *63*, 1031–1043.
45. Riedinger, A.; Pernia Leal, M.; Deka, S. R.; George, C.; Franchini, I. R.; Falqui, A.; Cingolani, R.; Pellegrino, T. "Nanohybrids" Based on pH-Responsive Hydrogels and Inorganic Nanoparticles for Drug Delivery and Sensor Applications. *Nano Lett.* **2011**, *11*, 3136–3141.
46. Alloyeau, D.; Oikawa, T.; Nelayah, J.; Wang, G.; Ricolleau, C. Following Ostwald Ripening in Nanoalloys by High-Resolution Imaging with Single-Atom Chemical Sensitivity. *Appl. Phys. Lett.* **2012**, *101*, 121920–121923.
47. Ricolleau, C.; Nelayah, J.; Oikawa, T.; Kohno, Y.; Braidy, N.; Wang, G.; Hue, F.; Alloyeau, D. High Resolution Imaging

and Spectroscopy Using CS-Corrected TEM with Cold FEG JEM-ARM200F. *JEOL News* **2012**, *47*, 2–8.
48. Alloyeau, D.; Ding, B.; Ramasse, Q.; Kisielowski, C.; Lee, Z.; Jeon, K.-J. Direct Imaging and Chemical Analysis of Unstained DNA Origami Performed with a Transmission Electron Microscope. *Chem. Commun.* **2011**, *47*, 9375–9377.
49. Fortin, J. P.; Wilhelm, C.; Servais, J.; Menager, C.; Bacri, J. C.; Gazeau, F. Size-Sorted Anionic Iron Oxide Nanomagnets As Colloidal Mediators for Magnetic Hyperthermia. *J. Am. Chem. Soc.* **2007**, *129*, 2628–2635.